GSA Data Repository 2017054

Bacterial sulfur disproportionation constrains timing of Neoproterozoic oxygenation

Marcus Kunzmann[1,2*], Thi Hao Bui[1], Peter W. Crockford[1], Galen P. Halverson[1], Clint Scott[3], Timothy W Lyons[4], Boswell A. Wing[1,5]

[1] Department of Earth & Planetary Sciences/GEOTOP, McGill University, 3450 University Street, Montréal, Québec H3A 0E8, Canada

[2] CSIRO Mineral Resources, Australian Resources Research Centre, 26 Dick Perry Avenue, Kensington, WA 6151, Australia and Northern Territory Geological Survey, Darwin, NT 0800, Australia

[3] United States Geological Survey, National Center, 12201 Sunrise Valley Drive, Reston, VA 20192, USA

[4] Department of Earth Sciences, University of California, Riverside, CA 92521-0423, USA

[5] Department of Geological Sciences, University of Colorado Boulder, UCB 399, Boulder, CO 80309-0399, USA

[*] Corresponding author: marcus.kunzmann@csiro.au

1 Geological setting

1.1 Svalbard

The Neoproterozoic succession in Svalbard represents one of the most complete sedimentary records of the middle to late Neoproterozoic and spans the 717-662 Ma Sturtian and 635 Ma Marinoan glaciations. Whereas the Veteranen Group at the base of the succession records an initial rift phase of basin development, the overlying Akademikerbreen and Polarisbreen groups were deposited on a stable continental shelf (Maloof et al., 2006). All sampled shales represent comparable depositional environments and were deposited at or just below storm wave base. Most samples come from the mixed siliciclastic-carbonate Polarisbreen Group because the Veteranen and Akademikerbreen groups are dominated by coarse siliciclastic and carbonate rocks, respectively. Cryogenian non-glacial samples were also sampled in East Greenland, where the Cryogenian interglacial Arena Formation represents the lateral equivalent of the MacDonaldryggen Member in Svalbard. Both units were deposited in a single and continuous basin (Fairchild and Hambrey, 1995).

1.2 Belt Supergroup

The Belt Supergroup of the northwestern United States and Canada was likely deposited in a restricted marine setting (Lyons et al., 2000). The age of the lower part of the succession has been constrained to be between 1470 and 1440 Ma (Anderson and Davis, 1995; Aleinikoff et al., 1996; Sears et al., 1998; Luepke and Lyons, 2001). Samples included in this study come from the Newland Formation, a unit in the lower part of the Belt Supergroup. The samples come from the Helena Embayment, the easternmost extension of the Belt Supergroup where no evidence for metamorphism is observable (Harrison, 1972; Schieber, 1989). The samples studied here were previously described in Lyons et al. (2000). They are microlaminated, organic-rich black shales that are interbedded with cm-scale, muddy turbidites, and represent deep-water deposition. More detailed information on the Belt Supergroup can be found in Winston (1986, 1990) and Winston and Link (1993).

1.3 Black Canyon River Dolomite

We analyzed three organic-rich shale samples from the Julius River Member of the Black River Dolomite in Tasmania. All samples are from drill core Forest 1. The Julius River Member represents a diamictite succession with an intercalated carbonate unit within the Black River Dolomite. Re-Os dating of black shales overlying the diamictite succession provides an age of 640±4.7 Ma for the upper Black River Dolomite (Kendall et al., 2009). The Black River Dolomite is overlain by the Croles Hill diamictite, which was previously correlated with Marinoan glacials in King Island (Cottons breccia) and South Australia (Elatina Formation), suggesting that the Julius River diamictite is Sturtian in age (Kendall et al., 2009). However, a recent U-Pb age of 636.41±0.45 Ma for the Cottons Breccia in Tasmania indicates its Marinoan age (Calver et al., 2013). This suggests that the Re-Os age from the Black River Dolomite correlates with the global 635 Ma Marinoan glaciation (Rooney et al., 2014). As our samples are interbedded with the diamictite, we suggest that they were deposited during the early stages of deglaciation from the Marinoan glaciation.

1.4 Sheepbed Formation, NW Canada

Ediacaran strata in NW Canada are exposed in the Ogilvie Mountains, the Wernecke Mountains, and the Mackenzie Mountains. The succession has traditionally been envisioned to have been deposited along an open, continental margin that developed in response to rifting of Rodinia about 780 to 700 Ma ago (e.g., Eisbacher, 1981; Jefferson and Parrish, 1989). However, recent studies suggest a more complex tectonostratigraphic evolution based on major facies changes (Aitken and Narbonne, 1989; Narbonne and Aitken, 1995), large overlapping unconformities (MacNaughton et al., 2000), and late Ediacaran syn-rift volcanics in the southeastern Canadian Cordillera (Colpron et al., 2002). The Sheepbed samples studied here come from a ca. 450-m-thick section (section M106 in Macdonald et al., 2013) at NE Profeit, Wernecke Mountains. Here, the Sheepbed Formation conformably overlies the post-Marinoan Raventhroat cap dolostone (Macdonald et al., 2013). The Sheepbed Formation comprises hundreds of meters of fissile black shale. Samples included in this study come from the lower ~100 m of the unit and are estimated to have been deposited between 635 and 630 Ma. Siltstone and carbonate beds are missing from the sampled interval and no evidence for deposition at or above storm wave base is present. A more detailed description of the Sheepbed Formation and the Ediacaran succession in NW Canada can be found in Macdonald et al. (2013).

1.5 A global signal of bacterial sulfur disproportionation

In order to evaluate the global importance of bacterial sulfur disproportionation, we measured the sulfur isotopic composition of post-Marinoan samples from three different basins. The basins are spread across Rodinia (Fig. DR1). All three sample sets show evidence of bacterial disproportionation of intermediate sulfur compounds.

2 Sulfur isotope analyses

Reduced inorganic sulfur in crushed shale samples was extracted by chromium reduction (Canfield et al., 1986). Depending on sulfur content, 0.2–15 g of sample powder was weighed into reaction vessels that were subsequently flushed with N_2. 15 ml of 6 M HCl was added

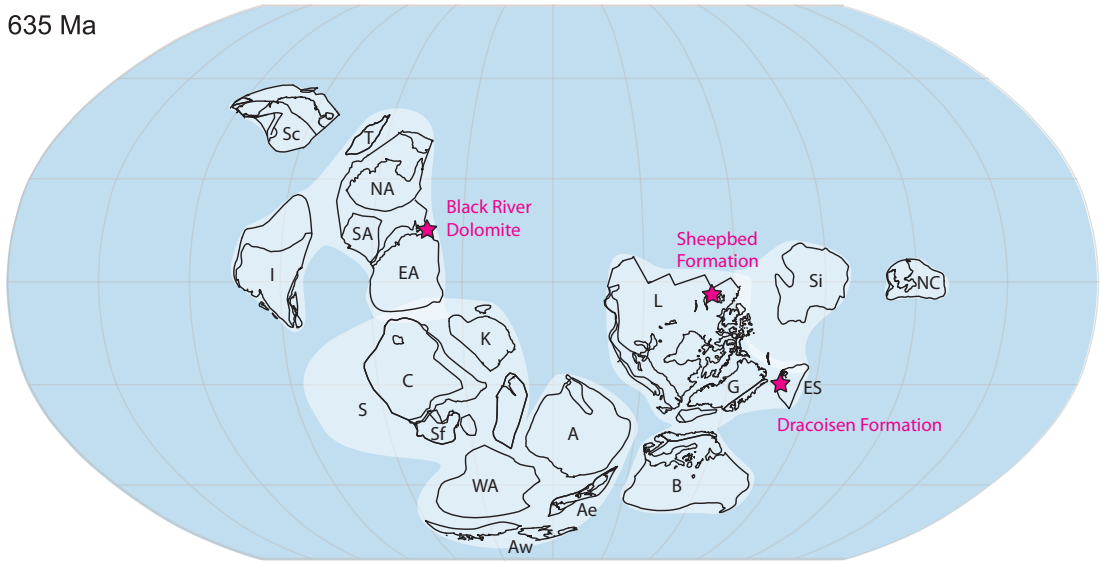

Fig. DR 1. A palaeogeographic reconstruction at ca. 635 Ma showing the location of measured post-Marinoan samples. A, Amazonia; Ae, Avalonia (east); Aw, Avalonia (west); B, Baltica; C, Congo; EA, East Antarctica; ES, East Svalbard; G, Greenland; I, India; K, Kalahari; L, Laurentia; NA, Northern Australia, NC, Northern China; S, Sahara; SA, South Australia; SC, South China; Sf, Sao Francisco; Si, Siberia; T, Tarim; WA, West Africa. Modified from Li et al. (2013).

to the reaction vessel, followed by 15 ml of 1 M chromic chloride solution prepared with 0.5 M HCl. The reaction vessels were heated to near-boiling and the reaction was performed for 2 h. Pyrite-sulfur, elemental sulfur, and acid-volatile monosulfides (AVS) are reduced to H_2S. Regular tests by adding only 6 M HCl assured that AVS did not occur in our samples (as common in ancient shales; Sperling et al., 2013). The N_2 carries the H_2S through a water trap (to remove acid contaminants) and finally through a zinc acetate solution (4% w/w). H_2S was quantitatively precipitated as ZnS. 1 ml 0.1 M $AgNO_3$ was added to the zinc acetate solution to convert the ZnS to Ag_2S. This reaction was carried out overnight in the dark. The Ag_2S was separated from solution by filtration on a 0.45 µm cellulose filter, attached to a 15 ml chimney, washed with one volume equivalent MQ-H_2O, one volume equivalent NH_4OH, and finally again with three volume equivalents MQ-H_2O. The Ag_2S was dried overnight at 80°C.

About 3 mg of Ag_2S were reacted in a nickel vessel overnight at about 250°C in the presence of excess F_2. The SF_6 generated was first purified by cryo-separation at -120°C. A second purification step was carried out by passing the SF_6 through two gas chromatography

columns ($\sim$2 m Haysep Q and $\sim$2 m Molsieve 5A) with ultrapure He as carrier gas at a rate of 20 ml/min. The SF_6 peak was isolated from contaminants and the carrier gas by trapping it on a cold finger at -192°C. The isotopic composition was measured on a ThermoFinniganMAT 253 dual-inlet gas-source isotope-ratio-mass-spectrometer. Sulfur isotope ratios were determined by measuring the ion beam intensities of $^{32}SF_5^+$, $^{33}SF_5^+$, $^{34}SF_5^+$, and $^{36}SF_5^+$ at mass to charge ratios (m/z) of 127, 128, 129, and 131.

All results are reported using delta notation relative to the Vienna-Cañon Diablo Troilite (V-CDT) international reference scale. On V-CDT scale, the $\delta^{34}S$ and $\Delta^{33}S$ values of the Ag_2S reference material, IAEA-S-1, are defined as -0.3‰ and 0.094‰, respectively (Ding et al., 2001). The reproducibility (1σ) of analyses (replicate samples) is estimated to be better than 0.1‰ and 0.015‰ for $\delta^{34}S$ and $\Delta^{33}S$, respectively.

Results from the Neoproterozoic succession in Svalbard are shown in Tab. DR1. Results from the Belt Supergroup (USA), the Black River Dolomite (Tasmania), Sheepbed Formation (Canada), and literature data from the Zaonega Formation (Russia) and Animikie Group (Canada) are shown in Tab. DR2.

Tab. DR 1. Total carbon (TC), total inorganic carbon (TIC), total organic carbon (TOC), S (all element data from Kunzmann et al. (2015)), and sulfur isotope data from Neoproterozoic shales in Svalbard. To avoid rounding errors, we report carbon data with two digits.

Section	Height	Unit	TC	TIC	TOC	S	$\delta^{33}S$	$\delta^{34}S$	$\delta^{36}S$	$\Delta^{33}S$	$\Delta^{36}S$
			wt.%	wt.%	wt.%	wt.%	‰	‰	‰	‰	‰
G306	159.0	Dracoisen	3.30	0.00	3.30	1.2	11.50	22.31	41.92	0.070	-0.892
G306	150.0	Dracoisen					3.17	6.17	11.73	-0.001	-0.037
G306a	143.0	Dracoisen	5.14	4.11	1.03	1.4	1.83	3.23	5.05	0.174	-1.091
G306	131.0	Dracoisen	1.23	0.00	1.23	1.1	2.36	4.14	7.54	0.232	-0.349
G436	138.0	Dracoisen	2.67	2.49	0.18	<0.1	-16.01	-30.95	-57.59	0.049	0.400
G436	120.0	Dracoisen	0.59	0.46	0.13	<0.1	-4.71	-9.56	-18.87	0.219	-0.786
G436	105.0	Dracoisen	1.28	0.76	0.52	1.2	-1.96	-4.10	-7.95	0.157	-0.163
G436	101.5	Dracoisen	0.88	0.27	0.61	0.6	-2.47	-5.16	-10.98	0.189	-1.188
G436	95.5	Dracoisen	0.74	0.48	0.27	0.3	1.61	2.80	3.98	0.170	-1.343
G436	88.0	Dracoisen	0.28	0.11	0.17	<0.1	2.41	4.33	6.97	0.180	-1.272
G436	64.0	Dracoisen	1.25	0.40	0.84	0.9	-10.78	-21.05	-40.55	0.119	-0.932
G436	42.0	Dracoisen	1.89	1.62	0.27	0.1	-17.04	-33.01	-61.53	0.099	0.262
G436	10.5	Dracoisen	0.95	0.39	0.56	1.1	-2.19	-4.56	-8.55	0.156	0.091
G411	72.0	Dracoisen	1.74	1.64	0.10	0.1	-0.01	-0.22	-1.16	0.103	-0.752
G411	67.0	Dracoisen	0.18	0.04	0.14	0.0					
G411	45.0	Dracoisen	4.73	4.56	0.17	0.1	-7.83	-15.26	-29.16	0.057	-0.360
G411	41.0	Dracoisen	5.63	5.48	0.14	0.4	-13.65	-26.43	-49.83	0.049	-0.213
G411	37.0	Dracoisen	2.40	2.11	0.30	<0.1	-13.88	-26.91	-51.22	0.068	-0.708
G419	2.6	Macdonald.	5.56	4.92	0.64	0.7	5.15	9.97	19.04	0.026	0.020
G419	6.7	Macdonald.	4.19	3.64	0.55	1.0	-1.91	-3.83	-6.80	0.059	0.455
G419	12.3	Macdonald.	2.95	2.25	0.71	0.9	4.11	8.00	15.07	-0.003	-0.195
G435	18.0	Macdonald.	1.28	1.06	0.22	0.1	-9.03	-17.55	-33.36	0.050	-0.274
G435	25.0	Macdonald.	2.47	2.23	0.24	0.3	-4.48	-8.71	-16.06	0.017	0.422
G435	35.0	Macdonald.	2.11	1.31	0.80	0.8	6.27	12.20	23.01	0.003	-0.306
G435	45.0	Macdonald.	1.69	0.86	0.83	0.9	12.74	24.92	48.10	-0.015	0.223
G435	56.0	Macdonald.	1.64	1.05	0.59	0.9	15.49	30.32	58.38	-0.016	-0.013

G435	66.0	Macdonald.	1.49	0.60	0.89	1.1	11.00	21.52	41.10	-0.024	-0.188
G435a	76.0	Macdonald.	2.37	1.69	0.68	1.3	13.71	26.84	51.57	-0.027	-0.047
G435	79.5	Macdonald.	2.34	1.82	0.52	0.9	17.46	34.22	65.88	-0.018	-0.133
G407	278.0	Macdonald.	1.75	1.56	0.19	0.0	2.16	4.20	7.69	0.000	-0.310
G407	261.0	Macdonald.	2.49	2.29	0.20	0.0	5.34	10.59	20.45	-0.100	0.227
G407	245.0	Macdonald.	2.78	2.55	0.23	<0.1	7.29	14.28	27.77	-0.041	0.472
G407	233.0	Macdonald.	2.92	2.68	0.24	0.0	6.25	12.38	24.11	-0.109	0.444
GR12	78.0	Arena			0.28	0.1					
GR12	71.0	Arena	0.66	0.47	0.20	1.0	17.26	33.95	65.88	-0.082	0.394
GR12	64.5	Arena	0.36	0.13	0.22	1.0	20.24	40.00	79.01	-0.163	1.646
GR12	15.9	Arena	0.22	0.00	0.22	1.0	15.07	29.63	57.14	-0.084	0.091
GR12	10.5	Arena	0.59	0.35	0.24	1.3	18.34	36.14	70.74	-0.112	0.963
GR12	8.5	Arena	0.73	0.35	0.38	2.0	17.95	35.49	69.13	-0.175	0.619
GR12	3.3	Arena	0.78	0.00	0.78	0.6	17.41	34.30	66.56	-0.109	0.390
G519	a	Russøya	0.29	0.00	0.29	0.0					
G519	b	Russøya	1.11	0.79	0.31	<0.1	3.66	7.16	13.33	-0.020	-0.313
G406	42.0	Russøya	1.42	0.00	1.42	0.2	-0.72	-1.45	-2.93	0.022	-0.177
G406	35.0	Russøya	1.75	0.06	1.69	0.2	0.15	0.21	-0.12	0.039	-0.514
G406	0.0	Russøya					16.77	32.94	63.49	-0.061	-0.017
G521	46.0	Russøya	0.31	0.00	0.31	<0.1	-4.10	-8.01	-15.34	0.027	-0.186
G521	44.4	Russøya	0.59	0.00	0.59	0.1	-4.74	-9.38	-18.27	0.096	-0.532
G521	40.5	Russøya	0.29	0.00	0.29	<0.1	-7.31	-14.19	-25.88	0.029	0.914
G521	36.0	Russøya	0.60	0.00	0.60	0.9	11.41	22.29	42.41	-0.006	-0.367
G521	33.0	Russøya	0.52	0.00	0.52	<0.1	2.83	5.55	11.15	-0.023	0.591
G521	30.0	Russøya	0.59	0.00	0.59	<0.1	15.12	29.35	56.47	0.107	-0.038
G521	26.4	Russøya	0.38	0.00	0.38	0.1	7.03	13.56	25.48	0.071	-0.432
G521	23.4	Russøya	0.77	0.05	0.71	<0.1	12.20	23.72	45.31	0.052	-0.243
G521	19.6	Russøya	0.92	0.00	0.92	0.1	5.22	10.11	20.66	0.025	1.367
G521	18.9	Russøya	1.44	0.00	1.44	0.1	3.97	7.63	13.97	0.053	-0.568
G521	13.2	Russøya	1.78	0.01	1.77	0.2					
G521	6.2	Russøya	1.06	0.00	1.06	0.0					

G521	3.7	Russøya	0.80	0.00	0.80	0.0					
P5014	52.0	Russøya					-3.61	-6.96	-12.93	-0.015	0.256
P5014	43.5	Russøya					-0.70	-1.45	-2.26	0.042	0.489
P5014	30.5	Russøya					6.92	13.60	25.99	-0.067	-0.019
G517		Backlund.	0.69	0.00	0.69	<0.1	-6.67	-12.92	-24.54	0.006	-0.142
G512	60.5	Svanberg.			0.63	0.0					
G512	55.0	Svanberg.	1.38	0.00	1.38	0.1	0.40	0.71	0.78	0.032	-0.583
G512	47.9	Svanberg.	0.83	0.14	0.69	<0.1	0.81	1.55	2.85	0.018	-0.093
G512	40.6	Svanberg.	0.19	0.00	0.19	0.0					
G512	35.2	Svanberg.	0.73	0.00	0.73	0.1	-1.83	-3.76	-7.44	0.104	-0.317
G512	26.2	Svanberg.	2.38	0.00	2.38	0.5	-3.04	-6.01	-12.12	0.064	-0.720
G512	24.1	Svanberg.	1.89	0.16	1.73	<0.1	-7.72	-14.91	-27.75	-0.010	0.382
G512	21.2	Svanberg.	0.81	0.00	0.81	1.6	-5.36	-10.23	-18.81	-0.082	0.534
G471	8.3	Svanberg.	0.30	0.01	0.30	0.0					
G471	6.1	Svanberg.	0.35	0.00	0.35	0.0					
G155	149.3	Svanberg.	0.09	0.00	0.09	<0.1	-12.61	-24.45	-47.06	0.056	-1.122
G155	149.1	Svanberg.	9.30	7.58	1.72	0.2	-10.08	-19.67	-37.18	0.104	-0.126
G155	133.5	Svanberg.			0.25	0.0					
G155	83.6	Svanberg.	5.84	5.56	0.28	0.1	-3.74	-7.28	-13.90	0.018	-0.109
G426	a	Veteranen	0.21	0.00	0.21	<0.1	-13.25	-25.68	-49.33	0.061	-1.099
G426	b	Veteranen	0.15	0.00	0.15	0.1					

Tab. DR 2. Multiple sulfur isotope data from non-euxinic samples from the Zaonega Formation (Russia; Scott et al. (2014)), Newland Formation of the Belt Supergroup (USA; new data), the Animicki Group (Gunflint, Biwabik,Trommald, Mahnomen) in Canada (Johnston et al., 2006), the Julius River Member (Black River Dolomite) in Tasmania (new data), and the Sheepbed Formation (Canada; new data).

Sample	Unit	Lithology	Age	$\delta^{33}S$ ‰	$\delta^{34}S$ ‰	$\delta^{36}S$ ‰	$\Delta^{33}S$ ‰	$\Delta^{36}S$ ‰	Reference
C-5190-16	Upper Zaonega U1	shale	2.1-2.0 Ga		17.42		-0.05		Scott et al. (2014)
C-5190-83	Upper Zaonega U1	shale	2.1-2.0 Ga		15.41		-0.02		Scott et al. (2014)
C-5190-86.9	Upper Zaonega U1	shale	2.1-2.0 Ga		13.26		-0.04		Scott et al. (2014)
C-5190-92.5	Upper Zaonega U1	shale	2.1-2.0 Ga		15.87		-0.03		Scott et al. (2014)
C-5190-96	Upper Zaonega U1	shale	2.1-2.0 Ga		15.19		-0.03		Scott et al. (2014)
C-5190-100	Upper Zaonega U1	shale	2.1-2.0 Ga		15.92		-0.02		Scott et al. (2014)
C-5190-136.5	Upper Zaonega U1	shale	2.1-2.0 Ga		14.87		-0.05		Scott et al. (2014)
C-5190-146.6	Upper Zaonega U1	shale	2.1-2.0 Ga		13.86		0.00		Scott et al. (2014)
C-5190-156	Upper Zaonega U1	shale	2.1-2.0 Ga		5.72		0.00		Scott et al. (2014)
C-5190-184	Upper Zaonega U1	shale	2.1-2.0 Ga		16.42		-0.05		Scott et al. (2014)
C-5190-199	Upper Zaonega U1	shale	2.1-2.0 Ga		-3.93		0.01		Scott et al. (2014)
C-5190-230	Upper Zaonega U2	shale	2.1-2.0 Ga		-18.13		0.03		Scott et al. (2014)
C-5190-234.5	Upper Zaonega U2	shale	2.1-2.0 Ga		-19.10		0.04		Scott et al. (2014)
C-5190-238.5	Upper Zaonega U2	shale	2.1-2.0 Ga		-19.11		0.07		Scott et al. (2014)
C-5190-245	Upper Zaonega U2	shale	2.1-2.0 Ga		-17.94		0.04		Scott et al. (2014)
C-5190-248	Upper Zaonega U2	shale	2.1-2.0 Ga		-15.27		0.01		Scott et al. (2014)
C-5190-287.5	Upper Zaonega U2	shale	2.1-2.0 Ga		-18.18		0.01		Scott et al. (2014)
C-5190-292.5	Upper Zaonega U2	shale	2.1-2.0 Ga		-19.15		0.02		Scott et al. (2014)
C-5190-293.2	Upper Zaonega U2	shale	2.1-2.0 Ga		-19.19		0.03		Scott et al. (2014)
C-5190-295.6	Upper Zaonega U2	shale	2.1-2.0 Ga		-19.45		0.03		Scott et al. (2014)
C-175-36.9	Upper Zaonega U2	shale	2.1-2.0 Ga		22.19		-0.05		Scott et al. (2014)
T19	Gunflint	BIF	1.87 Ga		10.20		-0.034	0.51	Johnston et al. (2006)
R2	Gunflint	BIF	1.87 Ga		10.22		-0.009	0.57	Johnston et al. (2006)
T13	Gunflint	BIF	1.87 Ga		13.33		-0.046	0.76	Johnston et al. (2006)
S22	Gunflint	BIF	1.87 Ga		-0.50		-0.028	0.45	Johnston et al. (2006)
S21	Gunflint	BIF	1.87 Ga		-0.43		-0.003	0.26	Johnston et al. (2006)

S1	Gunflint	BIF	1.87 Ga		4.07		-0.008	0.32	Johnston et al. (2006)
B44	Biwabik	BIF	1.87 Ga		6.97		-0.032	0.19	Johnston et al. (2006)
B26	Biwabik	BIF	1.87 Ga		9.83		-0.056	0.44	Johnston et al. (2006)
B3	Biwabik	BIF	1.87 Ga		3.26		0.003	0.27	Johnston et al. (2006)
M13	Trommald	BIF	1.87 Ga		12.24		-0.051	0.49	Johnston et al. (2006)
M16	Trommald	BIF	1.87 Ga		15.53		-0.073	0.70	Johnston et al. (2006)
M24	Trommald	BIF	1.87 Ga		7.73		-0.048	0.54	Johnston et al. (2006)
M25	Trommald	BIF	1.87 Ga		8.05		-0.027	0.73	Johnston et al. (2006)
M27	Trommald	BIF	1.87 Ga		8.65		-0.051	0.70	Johnston et al. (2006)
M30	Mahnomen	BIF/Chert	1.87 Ga		9.71		-0.062	0.51	Johnston et al. (2006)
M31	Mahnomen	BIF/Chert	1.87 Ga		9.59		-0.052	1.03	Johnston et al. (2006)
M37	Mahnomen	BIF/Chert	1.87 Ga		13.58		-0.051	0.76	Johnston et al. (2006)
M-16-204.8	Newland	shale	1.47 Ga	1.07	1.96	3.13	0.056	-0.603	this study
M-16-204.85	Newland	shale	1.47 Ga	1.04	1.92	3.36	0.051	-0.283	this study
M-16-232.8	Newland	shale	1.47 Ga	2.19	4.17	7.23	0.045	-0.706	this study
M-16-285	Newland	shale	1.47 Ga	2.85	5.55	10.05	-0.002	-0.527	this study
M-16-286.5	Newland	shale	1.47 Ga	-0.15	-0.37	-0.99	0.040	-0.293	this study
M-16-313.6	Newland	shale	1.47 Ga	2.68	5.13	9.40	0.047	-0.360	this study
M-16-371.5	Newland	shale	1.47 Ga	2.72	5.22	9.52	0.037	-0.418	this study
M-16-372.5	Newland	shale	1.47 Ga	2.79	5.32	9.71	0.048	-0.425	this study
M-16-372.55	Newland	shale	1.47 Ga	2.83	5.41	9.84	0.050	-0.465	this study
M-16-495	Newland	shale	1.47 Ga	1.39	2.60	4.64	0.049	-0.301	this study
M-16-495.05	Newland	shale	1.47 Ga	1.36	2.58	4.68	0.031	-0.229	this study
M-16-495.11	Newland	shale	1.47 Ga	1.31	2.44	4.32	0.053	-0.316	this study
M-16-494.15	Newland	shale	1.47 Ga	1.29	2.44	4.19	0.038	-0.445	this study
SC-93-538.6	Newland	shale	1.47 Ga	16.86	33.07	63.49	-0.041	-0.280	this study
SC-93-521.2	Newland	shale	1.47 Ga	13.85	27.08	51.79	-0.009	-0.286	this study
SC-93-526.8	Newland	shale	1.47 Ga	9.77	19.14	36.64	-0.044	-0.037	this study
SC-93-527	Newland	shale	1.47 Ga	9.56	18.66	35.20	-0.010	-0.552	this study
Forest I-894.9	Julius River	shale	0.64 Ga	-5.69	-11.58	-23.51	0.286	-1.626	this study
Forest I-914.9	Julius River	shale	0.64 Ga	-11.47	-22.43	-43.06	0.145	-0.883	this study

Forest I-926.8	Julius River	shale	0.64 Ga	-16.27	-31.63	-59.77	0.154	-0.525	this study
M106-82.5	Sheepbed	shale	0.64 Ga	-6.45	-12.69	-24.91	0.110	-0.927	this study
M106-84.5	Sheepbed	shale	0.64 Ga	-3.01	-6.01	-12.42	0.096	-1.019	this study
M106-90.5	Sheepbed	shale	0.64 Ga	-5.00	-9.93	-19.94	0.125	-1.165	this study
M106-94.5	Sheepbed	shale	0.64 Ga	-2.12	-4.34	-9.44	0.117	-1.210	this study
M106-96.5	Sheepbed	shale	0.64 Ga	-3.67	-7.38	-15.28	0.143	-1.300	this study
M106-98.5	Sheepbed	shale	0.64 Ga	-3.09	-6.30	-13.39	0.158	-1.452	this study
M106-110	Sheepbed	shale	0.64 Ga	-0.87	-1.97	-5.00	0.150	-1.254	this study
M106-117	Sheepbed	shale	0.64 Ga	4.32	8.25	14.82	0.086	-0.904	this study
M106-123	Sheepbed	shale	0.64 Ga	1.61	2.87	4.22	0.137	-1.232	this study
M106-133	Sheepbed	shale	0.64 Ga	2.16	3.87	5.88	0.165	-1.494	this study

3 Sulfur isotope model

3.1 Pore water pyrite formation

All analyzed samples were deposited in oxic to anoxic-ferruginous environments. Therefore, we assume that pyrite formation predominately took place in pore waters with excess iron. We compiled published data from samples that were also deposited under oxic to anoxic-ferruginous conditions. Iron speciation, redox-sensitive trace metal concentration or, if available, both types of data were used to constrain redox conditions during deposition. Redox data are listed in Tab. DR3 and iron speciation data are also presented in Fig. DR2. We do not show redox data from samples of the Animickie Group (Johnston et al., 2006) because all samples are banded iron formation (BIF), suggesting that pyrites were formed in pore waters with excess iron.

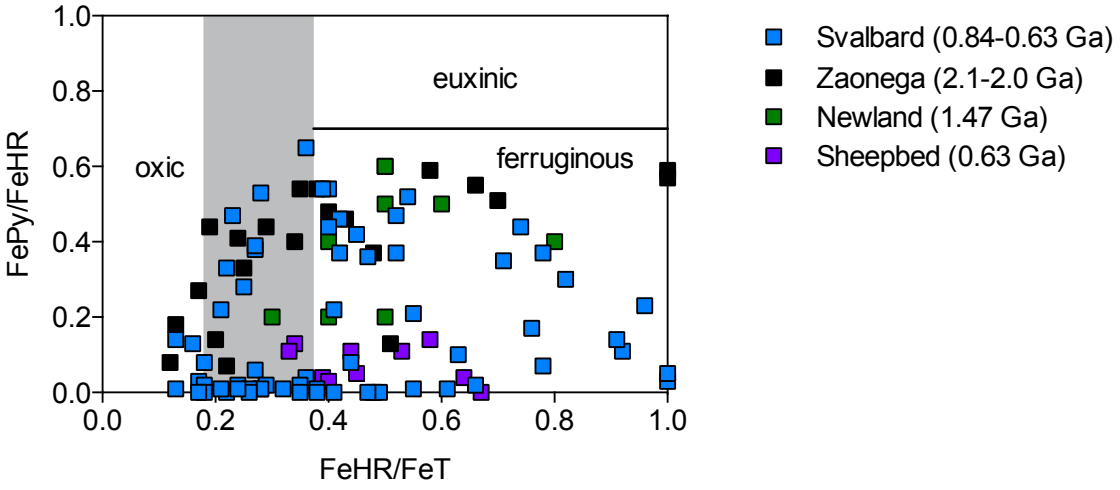

Fig. DR 2. Iron speciation data from samples analyzed in this study and complied data. Data are from Planavsky et al. (2011); Scott et al. (2014) and Kunzmann et al. (2015). Samples with an FeHR/FeT ratio between 0.18 and 0.38 were either deposited in anoxic or oxic environments. Mass balance requirements dictate that not all anoxic samples can be enriched in highly reactive iron. Enrichments can also be muted by rapid sedimenation (Poulton and Canfield, 2011).

Tab. DR 3. Iron speciation and redox-sensitive trace metal data from newly analyzed samples and literature data (Planavsky et al., 2011; Scott et al., 2014; Kunzmann et al., 2015)). All samples were deposited in non-euxinic environments. Samples from the Animickie Group (Johnston et al., 2006) are not listed because they are BIF, which implies that they were deposited under non-euxinic conditions.

Sample	Unit	FeHR/FeT	FePy/FeHR	Mo	U	V	Reference
				ppm	ppm	ppm	
G306-159	Dracoisen	0.82	0.30	17.0	6.5	170.8	Kunzmann et al. (2015)
G306-150.0	Dracoisen			5.8	3.6	120.1	Kunzmann et al. (2015)
G306a-143.0	Dracoisen	0.71	0.35	5.5	5.7	142.1	Kunzmann et al. (2015)
G306-131	Dracoisen	0.52	0.37	5.1	5.4	184.5	Kunzmann et al. (2015)
G436-138	Dracoisen	0.36	0.04	0.4	9.6	638.3	Kunzmann et al. (2015)
G436-120	Dracoisen	0.17	0.03	0.3	3.7	99.1	Kunzmann et al. (2015)
G436-105.0	Dracoisen	0.23	0.47	8.5	4.7	146.0	Kunzmann et al. (2015)
G436-101.5	Dracoisen	0.40	0.54	2.4	5.5	152.7	Kunzmann et al. (2015)
G436-95.5	Dracoisen	0.21	0.22	0.4	5.0	113.4	Kunzmann et al. (2015)
G436-88.0	Dracoisen	0.13	0.14	0.7	5.2	108.2	Kunzmann et al. (2015)
G436-64.0	Dracoisen	0.45	0.42	1.2	4.9	114.8	Kunzmann et al. (2015)
G436-42.0	Dracoisen	0.41	0.22	0.4	8.4	622.5	Kunzmann et al. (2015)
G436-10.5	Dracoisen	0.18	0.08	2.3	4.9	128.0	Kunzmann et al. (2015)
G411-72.0	Dracoisen	0.27	0.06	0.2	2.1	66.4	Kunzmann et al. (2015)
G411-67.0	Dracoisen	0.22	0.00	0.2	2.8	97.5	Kunzmann et al. (2015)
G411-45.0	Dracoisen	0.61	0.01	0.1	2.0	45.8	Kunzmann et al. (2015)
G411-42.0	Dracoisen	0.63	0.10	0.4	1.7	31.7	Kunzmann et al. (2015)
G411-37.0	Dracoisen	0.35	0.02	0.2	3.0	84.7	Kunzmann et al. (2015)
G419-2.6	Macdonald.	0.78	0.37	0.6	2.2	38.7	Kunzmann et al. (2015)
G419-6.7	Macdonald.	0.74	0.44	1.0	2.3	52.0	Kunzmann et al. (2015)
G419-12.3	Macdonald.	0.54	0.52	1.6	2.1	72.7	Kunzmann et al. (2015)
G435-18.0	Macdonald.			0.2	2.9	75.6	Kunzmann et al. (2015)
G435-25.0	Macdonald.	0.55	0.21	0.7	2.3	61.8	Kunzmann et al. (2015)
G435-35.0	Macdonald.	0.47	0.36	0.4	3.0	90.7	Kunzmann et al. (2015)
G435-45.0	Macdonald.	0.42	0.37	0.5	2.8	107.4	Kunzmann et al. (2015)
G435-56.0	Macdonald.	0.39	0.54	0.5	3.1	111.9	Kunzmann et al. (2015)

G435-66.0	Macdonald.	0.52	0.47	0.5	3.0	107.6	Kunzmann et al. (2015)
G435a-76.0	Macdonald.	0.42	0.46	0.5	2.6	100.2	Kunzmann et al. (2015)
G435-79.5	Macdonald.	0.40	0.44	0.4	2.6	106.8	Kunzmann et al. (2015)
G407-278.0	Macdonald.	0.24	0.02	0.1	2.1	131.5	Kunzmann et al. (2015)
G407-261.0	Macdonald.	0.28	0.01	0.2	1.9	141.0	Kunzmann et al. (2015)
G407-245.0	Macdonald.	0.29	0.02	0.1	2.0	140.9	Kunzmann et al. (2015)
G407-233.0	Macdonald.	0.28	0.01	0.2	1.7	128.3	Kunzmann et al. (2015)
GR12-78.0	Arena	0.16	0.13	0.2	1.7	175.7	Kunzmann et al. (2015)
GR12-71.0	Arena	0.27	0.38	0.2	1.5	157.5	Kunzmann et al. (2015)
GR12-64.5	Arena	0.22	0.33	0.8	1.8	193.5	Kunzmann et al. (2015)
GR12-15.9	Arena	0.27	0.39	0.2	1.9	173.3	Kunzmann et al. (2015)
GR12-10.5	Arena	0.28	0.53	0.4	1.9	182.9	Kunzmann et al. (2015)
GR12-8.5	Arena	0.36	0.65	0.8	2.0	194.3	Kunzmann et al. (2015)
GR12-3.3	Arena	0.76	0.17	5.1	0.5	50.9	Kunzmann et al. (2015)
G519a	Russøya	0.35	0.00	0.3	2.2	94.8	Kunzmann et al. (2015)
G519b	Russøya	0.18	0.02	0.2	2.0	145.7	Kunzmann et al. (2015)
G406-42.0	Russøya	0.92	0.11	0.4	1.1	22.6	Kunzmann et al. (2015)
G406-35.0	Russøya	0.78	0.07	1.0	2.0	40.4	Kunzmann et al. (2015)
G406-0.0	Russøya			0.1	0.6	1.5	Kunzmann et al. (2015)
G521-46.0	Russøya	0.38	0.01	0.4	2.9	59.5	Kunzmann et al. (2015)
G521-44.4	Russøya	0.55	0.01	0.5	2.4	63.4	Kunzmann et al. (2015)
G521-40.5	Russøya	0.21	0.01	0.2	2.4	57.9	Kunzmann et al. (2015)
G521-36.0	Russøya	0.25	0.28	0.5	2.4	55.1	Kunzmann et al. (2015)
G521-33.0	Russøya	0.26	0.01	0.3	2.0	63.4	Kunzmann et al. (2015)
G521-30.0	Russøya	0.48	0.00	0.7	2.2	57.1	Kunzmann et al. (2015)
G521-26.4	Russøya	0.49	0.00	1.1	2.8	54.1	Kunzmann et al. (2015)
G521-23.4	Russøya	0.18	0.00	0.4	2.4	55.5	Kunzmann et al. (2015)
G521-19.6	Russøya	0.32	0.01	0.4	2.1	61.0	Kunzmann et al. (2015)
G521-18.9	Russøya	1.11	0.03	0.2	3.9	72.4	Kunzmann et al. (2015)
G521-13.2	Russøya	0.41	0.00	0.9	2.3	57.9	Kunzmann et al. (2015)
G521-6.2	Russøya	0.47	0.00	0.4	3.5	79.8	Kunzmann et al. (2015)

G521-3.7	Russøya			0.5	2.5	63.3	Kunzmann et al. (2015)
P5014-52.0	Russøya			0.1	0.6	4.4	Kunzmann et al. (2015)
P5014-43.5	Russøya			0.2	0.7	2.7	Kunzmann et al. (2015)
P5014-30.5	Russøya			0.1	0.5	1.3	Kunzmann et al. (2015)
G517	Backlund.	0.44	0.08	0.5	1.1	43.4	Kunzmann et al. (2015)
G512-55.0	Svanberg.	0.66	0.02	1.6	2.5	51.5	Kunzmann et al. (2015)
G512-40.6	Svanberg.	0.38	0.00	0.7	4.5	119.2	Kunzmann et al. (2015)
G512-35.2	Svanberg.	1.05	0.05	1.7	2.5	50.7	Kunzmann et al. (2015)
G512-26.2	Svanberg.			1.0	2.6	49.9	Kunzmann et al. (2015)
G471-8.3	Svanberg.			0.5	3.0	131.5	Kunzmann et al. (2015)
G471-6.1	Svanberg.	0.26	0.00	0.6	2.1	167.5	Kunzmann et al. (2015)
G155-149.3	Svanberg.	0.24	0.01	0.2	1.3	150.2	Kunzmann et al. (2015)
G155-149.1	Svanberg.	0.91	0.14	1.2	2.1	67.8	Kunzmann et al. (2015)
G155-133.5	Svanberg.	0.96	0.23	0.6	0.4	9.2	Kunzmann et al. (2015)
G155-83.6	Svanberg.			0.5	0.7	86.6	Kunzmann et al. (2015)
G426a	Veteranen	0.13	0.01	0.2	2.6	72.9	Kunzmann et al. (2015)
G426b	Veteranen	0.17	0.00	0.2	4.2	132.4	Kunzmann et al. (2015)
C-5190-16	Upper Zaonega U1	0.17	0.27				Scott et al. (2014)
C-5190-83	Upper Zaonega U1	0.70	0.51				Scott et al. (2014)
C-5190-86.9	Upper Zaonega U1	1.02	0.57				Scott et al. (2014)
C-5190-92.5	Upper Zaonega U1	0.51	0.13				Scott et al. (2014)
C-5190-96	Upper Zaonega U1	0.34	0.40				Scott et al. (2014)
C-5190-100	Upper Zaonega U1	0.43	0.46				Scott et al. (2014)
C-5190-136.5	Upper Zaonega U1	0.22	0.07				Scott et al. (2014)
C-5190-146.6	Upper Zaonega U1	0.38	0.54				Scott et al. (2014)
C-5190-156	Upper Zaonega U1	0.35	0.54				Scott et al. (2014)
C-5190-184	Upper Zaonega U1	0.24	0.41				Scott et al. (2014)
C-5190-199	Upper Zaonega U1	0.58	0.59				Scott et al. (2014)
C-5190-230	Upper Zaonega U2	0.48	0.37				Scott et al. (2014)
C-5190-234.5	Upper Zaonega U2	0.25	0.33				Scott et al. (2014)
C-5190-238.5	Upper Zaonega U2	0.12	0.08				Scott et al. (2014)

C-5190-245	Upper Zaonega U2	0.40	0.48				Scott et al. (2014)
C-5190-248	Upper Zaonega U2	0.13	0.18				Scott et al. (2014)
C-5190-287.5	Upper Zaonega U2	0.19	0.44				Scott et al. (2014)
C-5190-292.5	Upper Zaonega U2	0.29	0.44				Scott et al. (2014)
C-5190-293.2	Upper Zaonega U2	0.66	0.55				Scott et al. (2014)
C-5190-295.6	Upper Zaonega U2	0.20	0.14				Scott et al. (2014)
C-175-36.9	Upper Zaonega U2	1.04	0.59				Scott et al. (2014)
M-16-204.8	Newland	0.50	0.60				Planavsky et al. (2011)
M-16-204.85	Newland	0.50	0.50				Planavsky et al. (2011)
M-16-232.8	Newland	0.40	0.40				Planavsky et al. (2011)
M-16-313.6	Newland	0.50	0.60				Planavsky et al. (2011)
M-16-495	Newland	0.8	0.4				Planavsky et al. (2011)
M-16-495.05	Newland	0.6	0.5				Planavsky et al. (2011)
SC-93-521.2	Newland	0.3	0.2				Planavsky et al. (2011)
SC-93-526.8	Newland	0.4	0.2				Planavsky et al. (2011)
SC-93-527	Newland	0.5	0.2				Planavsky et al. (2011)
Forest I-894.9	Julius River			6	1.9	96	this study
Forest I-914.9	Julius River			4	3.4	180	this study
Forest I-926.8	Julius River			10	12.4	149	this study
M106-82.5	Sheepbed	0.39	0.04				this study
M106-84.5	Sheepbed	0.40	0.03				this study
M106-90.5	Sheepbed	0.34	0.13				this study
M106-94.5	Sheepbed	0.45	0.05				this study
M106-96.5	Sheepbed	0.33	0.11				this study
M106-98.5	Sheepbed	0.44	0.11				this study
M106-110	Sheepbed	0.53	0.11				this study
M106-117	Sheepbed	0.67	0.00				this study
M106-123	Sheepbed	0.64	0.04				this study
M106-133	Sheepbed	0.58	0.14				this study

3.2 General assumptions

All analyzed and compiled multiple sulfur isotope data are from samples deposited in non-euxinic environments (Fig. DR2, Tab. DR3). Therefore, we assume that pyrites were formed in pore waters in the presence of excess iron. Thus, we assume rapid and irreversible pyrite formation, and, if present, rapid bacterial sulfur disproportionation (BSD). We model the isotopic composition of pyrites based on a model for sulfate concentration in pore waters (Berner, 1964). This model assumes steady state conditions and that the initial concentration of sulfate in pore waters at a specific depth mostly reflects the sum of three processes: diffusion, deposition plus compaction, and microbial sulfate reduction (MSR) (Berner, 1964):

$$SO4_z = (SO4_0 - SO4_\infty) exp\left[-\frac{k}{\omega} z\right] + SO4_\infty \quad (1)$$

where

$SO4_z$=concentration of sulfate at any given depth

$SO4_0$=initial sulfate concentration

$SO4_\infty$=concentration of sulfate at infinitive depth, i.e. sulfate left after MSR

k=sulfate reduction rate constant

ω=rate of sediment deposition

Because $SO4_z$ (total) = $^{32}SO4_z$ + $^{33}SO4_z$ + $^{34}SO4_z$ + $^{36}SO4_z$, equation (1) can be re-written for the isotope of interest, ignoring ^{36}S due to its low abundance of only 0.02% (Rosman and Taylor, 1998), and the isotopic composition of sulfate at any given depth is

$$\delta^{3i}S_{SO4} = \left[\frac{\left(\frac{^{3i}SO4}{^{32}SO4}\right)}{\left(\frac{^{3i}S}{^{32}S}\right)_{CDT}} - 1 \right] \cdot 1000 \quad (2)$$

here i equals 3, or 4.

3.3 The sulfur isotope composition of pore water sulfate and the sulfur isotope fractionation factor

The δ^{3i}S of pore water sulfate is a function of δ^{3i}S composition of seawater at the seafloor, sulfate reduction rate constant (k), sedimentation rate (ω) and S isotope fractionation factor (α) produced by sulfate reducing bacteria. This fractionation factor is defined as the ratio of sulfate reduction rate (SRR) of less abundant isotopes (^{33}S or ^{34}S) over the abundant isotope ^{32}S normalized with corresponding isotope concentration

$$^{3i}\alpha = \frac{\left(\frac{^{3i}SRR}{^{3i}\mathrm{S}}\right)}{\left(\frac{^{32}SRR}{^{32}\mathrm{S}}\right)}. \tag{3}$$

The Δ^{33}S of pore water sulfate is calculated based on δ^{33}S, δ^{34}S and the slope $^{33}\lambda$ of the terrestrial mass fractionation line

$$\Delta^{33}\mathrm{S}_{SO4} = \delta^{33}\mathrm{S}_{SO4} - 1000 \cdot \left[\left(1 + \frac{\delta^{34}\mathrm{S}_{SO4}}{1000}\right)^{^{33}\lambda} - 1\right]. \tag{4}$$

3.4 The sulfur isotopic composition of pore water sulfide and pyrite

The S isotopic composition of instantaneous H_2S produced by sulfate reducing bacteria is calculated using ratios of sulfate reduction rates at corresponding depth

$$\delta^{3i}\mathrm{H}_2S = \left[\frac{\left(\frac{^{3i}SRR}{^{32}SRR}\right)}{\left(\frac{^{3i}\mathrm{S}}{^{32}\mathrm{S}}\right)_{CDT}} - 1\right] \cdot 1000. \tag{5}$$

Pyrites preserve the isotope signature of accumulated H_2S, which varies from instantaneous H_2S composition to seawater sulfate composition (when all sulfate is reduced to sulfide).

3.5 Model parameters, model runs, results

We can account for the isotopic consequences of a re-oxidative sulfur cycle, i.e. bacterial disproportionation of intermediate sulfur compounds. A contribution of a re-oxidative sulfur cycle to the final composition of pyrite would result in $^{33}\lambda_{net}$ (representing the combined

effects of MSR and BSD) values >0.5145 (Farquhar et al., 2003; Johnston et al., 2005; Sim et al., 2011a). Tab. DR4 summarizes the used parameters in our numerical model and Fig. DR3 shows a graphical representation of the model.

Tab. DR 4. Summary of the parameters used in the model. α_{net} represents the combined effects of MSR and potential BSD. λ_{net} was only treated as free parameter in the second model runs. In the first model runs, it was set to 0.513.

Fixed parameters	Value	Free parameters	Value
α_{net}	0.95	$\delta^{34}S$	10–40‰
k/ω	0.1/cm	$\Delta^{33}S$	-0.2–0.1‰
SO4(0)	28 mM	$^{33}\lambda_{net}$	0.511–0.518

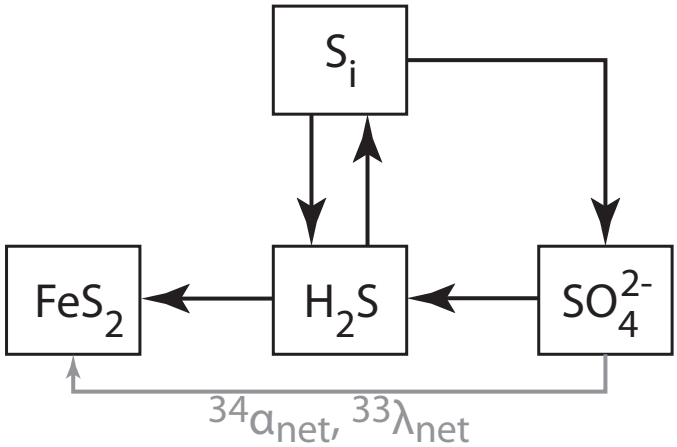

Fig. DR 3. Conceptual model of our pore water sulfur model. The four boxes correspond to the sulfate, hydrogen sulfide, intermediate sulfur compound, and pyrite pools. Black arrows represent sulfur fluxes. The grey arrow indicates the net fractionation factors ($^{34}\alpha_{net}$, $^{33}\lambda_{net}$) that includes the combined fractionations during MSR and BSD.

By considering a range for $\delta^{34}S$ and $\Delta^{33}S$ values for the starting composition of seawater sulfate, we indirectly include the impact of varying Proterozoic sulfate concentrations. Changing sulfate concentrations, however, do not directly affect our results as they simply control the depth of sulfate penetration for a given pair of k/ω values. This simply controls where in the sediment column pyrite would be produced but does not affect its predicted isotopic compositions.

3.6 Sensitivity tests

We performed additional sensitivity tests to explore the effects of variation in α_{net} (Fig. DR4) and k/ω (Fig. DR5).

We varied α_{net} between 0.97 and 0.93 (Fig. DR4), using the same $\delta^{34}S$ and $\Delta^{33}S$ values for the starting sulfate composition and a λ_{net} of 0.513. In contrast to our preferred α_{net} of 0.95 (Fig. 2; DR4b), an α_{net} of 0.97 is too small to reproduce most of our data (Fig. DR4a). As expected, an α_{net} of 0.97, i.e. an ϵ_{net} of 70‰ (the highest possible fractionation between sulfate and sulfide, which is rarely observed), produces a very large model field (Fig. DR4c). However, it does not reproduce the trend in our pre-Marinoan data set. Furthermore, the post-Marinoan data from the Dracoisen Formation can only be reproduced when the composition of the starting seawater sulfate is set to have negative $\delta^{34}S$ and $\Delta^{33}S$ (Fig. DR4c). Such a composition is inconsistent with the recently determined positive $\delta^{34}S$ and $\Delta^{33}S$ composition of the post-Marinoan seawater sulfate reservoir (Crockford et al., 2016; Sansjofre et al., 2016). Therefore, we conclude that an α_{net} of 0.95 produces the best model solution. Using an α_{net} of 0.97 and setting the starting sulfate composition to values of the post-Marinoan sulfate reservoir, the model is not able to reproduce either the pre- or post-Marinoan data (Fig. DR4d).

Although difficult to constrain in ancient environments, we assume a k/ω of 0.1 considering the depositional environment of our samples. This value compares well with data compiled by Canfield (1989). Varying k/ω between 0.07 and 0.5 only leads to minor shifts in the isotopic composition of accumulated pyrite (Fig.DR5).

4 Estimating sulfide re-oxidation rate

We estimate the mininum sulfide oxidation rate with a recent model of re-oxidative sulfur cycling in sediments of Mangrove Lake, Bermuda (Fig. DR6; Pellerin et al., 2015). A graphical application of this model suggests a minimum sulfide re-oxidation of 80% (Fig. DR6). The model presented in Fig. DR6 also quantifies the proportion of the reaction solely caused by MSR ($^{34}\epsilon_{msr}$) to ca. 38‰, a value consistent with the most recent culture experiments (Leavitt et al., 2013).

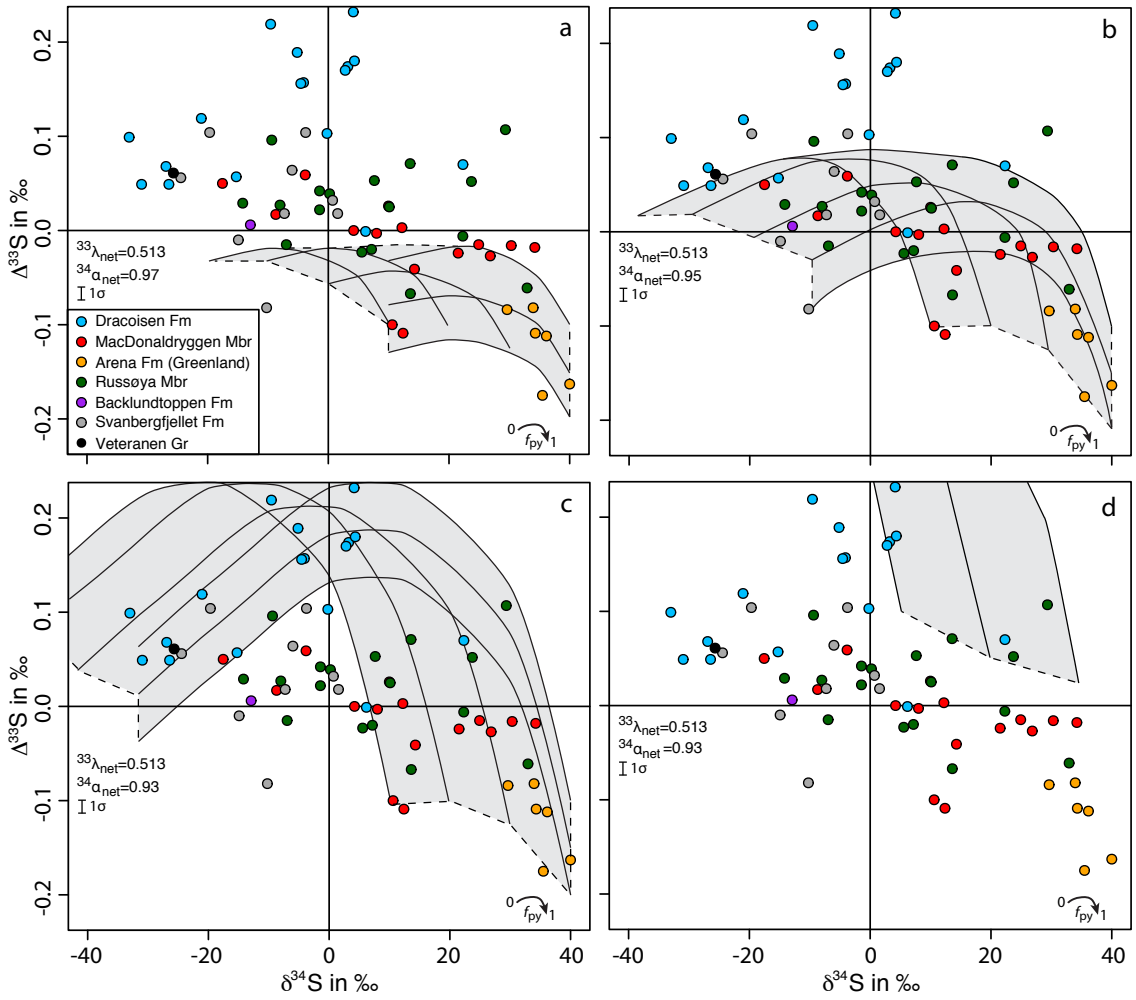

Fig. DR 4. Sensitivity test results exploring the effect of varying α_{net}. See text for discussion.

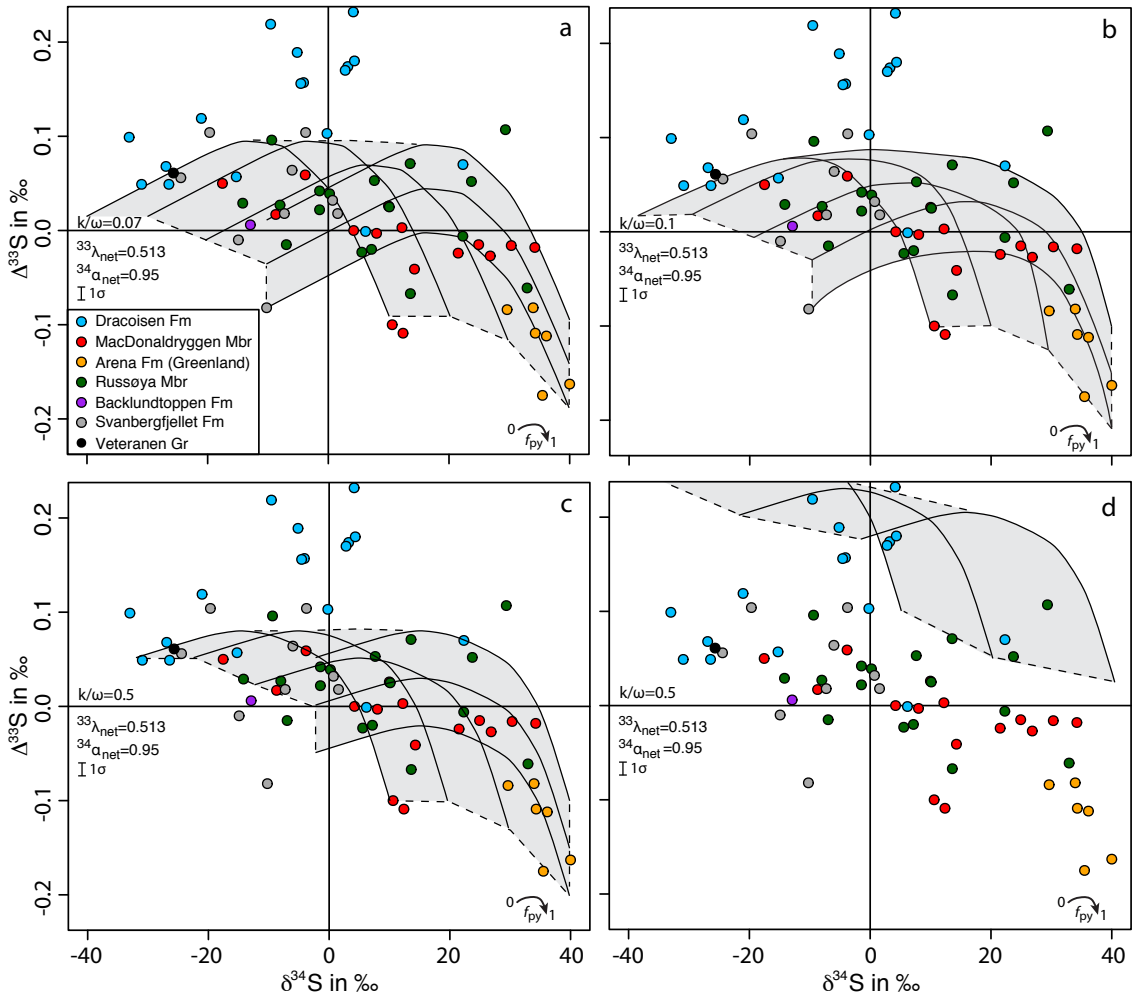

Fig. DR 5. Sensitivity test results exploring the effect of varying k/ω. See text for discussion.

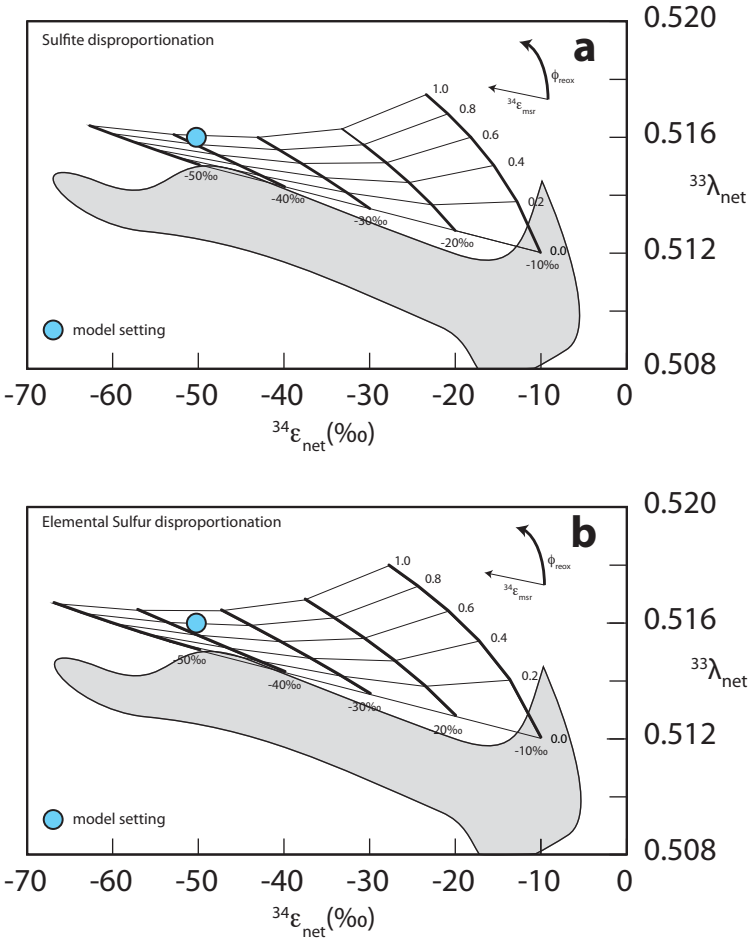

Fig. DR 6. Model for the re-oxidative sulfur cycle including disproportionation of sulfite (a) and elemental sulfur (b) (from Pellerin et al., 2015). The grey field represents isotopic fractionations by pure cultures of sulfate reducers (Johnston et al., 2005; Sim et al., 2011a,b; Leavitt et al., 2013). Arrows indicate the direction of increasing fractionation by microbial sulfate reduction $^{34}\epsilon_{msr}$ and fraction of sulfide re-oxidation (ϕ_{reox}). The x-axis shows the net fractionation ($^{34}\epsilon_{net}$), including sulfate reduction and sulfur disproportionation. The bold lines of the grid indicate the fractionation associated with microbial sulfate reduction alone, where the fraction of re-oxidation is zero. The other set of lines traces the flux of sulfide that is re-oxidized. We identify the fraction of re-oxidized sulfide by moving the grid to maximum $^{33}\lambda_{net}$ values observed for microbial sulfate reduction. The model indicates sulfide re-oxidation of >80%.

5 Rising Ediacaran seawater sulfate levels

We estimate the magnitude of rising Ediacaran seawater sulfate levels with a simple model developed by Canfield and Farquhar (2009). The model assumes steady state, i.e. that the flux of sulfur into the ocean equals the flux out:

$$Flux_{\text{in}} = Flux_{\text{out}} \tag{6}$$

Sulfur leaves the ocean either as evaporite deposits (sulfate) or as pyrite (sulfide). Pyrite burial depends on the production of sulfide through microbial sulfate reduction (MSR) and the proportion of this sulfide that becomes buried in the geological record, described by the factor x. This means:

$$Flux_{\text{out}} = xMSR + evap \tag{7}$$

where *evap* stands for the sulfur removed as evaporite deposits. MSR rate depends on the availability of reactive organic matter as electron donor and the concentration of sulfate. This gives:

$$MSR = aOC[SO_4]^y \tag{8}$$

where OC represents reactive organic carbon, a is a constant of proportionality, and y is an exponential factor. Equation 6–8 can be combined and as result a simple equation for seawater sulfate is generated:

$$[SO_4] = \left[\frac{[flux_{\text{in}} - evap]}{axOC}\right]^{1/y} \tag{9}$$

Canfield and Farquhar (2009) argue that the availability of reactive organic carbon unlikely changed much over the Precambrian, thus they ignore OC in equation 9. If the flux of sulfur into the ocean does not change, and the formation of evaporites is ignored, sulfate levels are controlled by the factors x and y. Considering the onset of a re-oxidative sulfur cycle at one point in time, the equation can be modified to:

$$\frac{[SO_4]_{\mathrm{i}}}{[SO_4]_{\mathrm{j}}} = \left(\frac{x_{\mathrm{j}}}{x_{\mathrm{i}}}\right)^{1/y} \tag{10}$$

where subscripts i and j denote *after* and *before* onset of a re-oxidative sulfur cycle, respectively. The size of the seawater sulfate reservoir, as well as the flux into the ocean, do not significantly change the magnitude of the increase in seawater sulfate concentration, they only change the response time to the onset of re-oxidative sulfur cycling (Canfield and Farquhar, 2009). Canfield and Farquhar (2009) point out that a reduction of x, i.e. lowering the proportion of sulfide buried, will inevitably lead to higher seawater sulfate levels. We assume a value of x_j of 1 before re-oxidative sulfur cycling, i.e. all sulfide produced by MSR is buried as pyrite. Although it is difficult to constrain Neoproterozoic values for x, Canfield and Farquhar (2009) suggest a value around 0.2, based on their model. Therefore, we use this value for x_i. y is a factor of proportionality between seawater sulfate concentration and sulfate reduction rate. A y value of 1 means that sulfate reduction rate responds linearly to sulfate concentration, i.e. increasing sulfate concentration by a factor of 2 will double the sulfate reduction rate. However, in nature this is not true because sulfate reduction rate does also depend on the availability of reactive organic matter as electron donor. This means that realistic y values are less than 1. Garrels and Lerman (1981) identified that a y value of 0.3 represents the best fit for the relationship between sulfate concentration and sulfate reduction rate. Varying the exponential factor y between 1 and 0.3 suggests an increase in seawater sulfate concentration by a factor of 5 and ∼200.

References

Aitken, J. D., Narbonne, G. M., 1989. Two Occurences of Precambrian Thrombolites from the Mackenzie Mountains, Northwestern Canada. Palaios 4, 384–388.

Aleinikoff, J. N., Evans, K. V., Fanning, C. M., Obradovich, J. D., Ruppel, E. T., Zeig, J. A., Steinmetz, J. C., 1996. SHRIMP U-Pb ages of felsic igneous rocks, Belt Supergroup, western Montana. In: GSA Ann. Mtg. Prog. Abst. 28, A 376.

Anderson, H. E., Davis, D. W., 1995. U-Pb geochronlogy of the Moyie sills, Purcell Supergroup, southeastern British Columbia: Implications for the Mesoproterozoic geological history of the Purcell (Belt) basin. Canadian Journal of Earth Sciences 32, 1180–1193.

Berner, R. A., 1964. An idealized model of dissolved sulfate distribution in recent sediments. Geochimica et Cosmochemica Acta 28, 1497–1503.

Calver, C. R., Crowley, J. L., Wingate, M. T. D., Evans, D. A. D., Raub, T. D., Schmitz, M. D., 2013. Globally synchronous Marinoan deglaciation ndicated by U-Pb geochronology of the Cottons Breccia, Tasmania, Australia. Geoloy 41, 1127–1130.

Canfield, D. E., 1989. Sulfate reduction and oxic respiration in marine sediments: implications for organic carbon preservation in euxinic environments. Deep Sea Research 36, 121–138.

Canfield, D. E., Farquhar, J., 2009. Animal evolution, bioturbation, and the sulfate concentration of the oceans. Proceedings of the National Academy of Sciences of the USA 106, 8123–8127.

Canfield, D. E., Raiswell, R., Westrich, J. T., Reaves, C. M., Berner, R. A., 1986. The use of chromium reduction in the analysis of reduced inorganic sulfur in sediments and shales. Chemical Geology 54, 149–155.

Colpron, M., Logan, J. M., Mortensen, J. K., 2002. U-Pb zircon age constraint for late Neoproterozoic rifting and initiation of lower Paleozoic passive margin of western Laurentia. Canadian Journal of Earth Sciences 39, 133–143.

Crockford, P. W., Cowie, B. R., Johnston, D. T., Hoffman, P. F., Sugiyama, I., Pellerin, A., Bui, T. H., Hayles, J., Halverson, G. P., Macdonald, F. A., Wing, B. A., 2016. Triple oxygen and multiple sulfur isotope constraints on the evolution of the post-Marinoan sulfur cycle. Earth and Planetary Science Letters 435, 74–83.

Ding, T., Valkiers, S., Kipphardt, H., Bièvre, D., Taylor, P. D. P., Gonfiantini, R., Krouse, R., 2001. Calibrated sulfur isotope abundance ratios of three IAEA sulfur isotope reference materials and V-CDT with a reassement of the atomic weight of sulfur. Geochimica et Cosmochemica Acta 65 (15), 2433–2437.

Eisbacher, G. H., 1981. Sedimentary tectonics and glacial record in the Windermere Supergroup, Mackenzie Mountains, northwestern Canada. Geolological Survey of Canada, Paper 80-27, 1–40.

Fairchild, I. J., Hambrey, M. J., 1995. Vendian basin evolution in East Greenland and NE Svalbard. Precambrian Research 73, 217–233.

Farquhar, J., Johnston, D. T., Wing, B. A., Habicht, K. S., Canfield, D. E., Airieau, S., Thiemens, M. H., 2003. Multiple sulphur isotopic interpretations of biosynthetic pathways: implications for biological signatures in the sulphur isotope record. Geobiology 1, 27–36.

Garrels, R. M., Lerman, A., 1981. Phanerozoic cycles of sedimentary carbon and sulfur. Proceedings of the National Acadamy of Sciences (USA) 78 (8), 4652–4656.

Harrison, J. E., 1972. Precambrian Belt basin of northwestern United States–It's geometry, sedimentation, and copper occurrences. Geological Society of America Bulletin 83, 1215–1240.

Jefferson, C. W., Parrish, R. R., 1989. Late Proterozoic stratigraphy, U-Pb zircon ages, and rift tectonics, Mackenzie Mountains, northwestern Canada. Canadian Journal of Earth Sciences 26, 1784–1801.

Johnston, D. T., Farquhar, J., Wing, B. A., Kaufman, A. J., Canfield, D. E., Habicht, K. S., 2005. Multiple sulfur isotope fractionations in biological systems: a case study

with sulfate reducers and sulfur disproportionaters. American Journal of Science 305, 645–660.

Johnston, D. T., Poulton, S. W., Fralick, P. W., Wing, B. A., Canfield, D. E., Farquhar, J., 2006. Evolution of the oceanic sulfur cycle at the end of the Paleoproterozoic. Geochimica et Cosmochemica Acta 70, 5723–5739.

Kendall, B., Creaser, R. A., Calver, C. R., Raub, T. D., Evans, D. A. D., 2009. Correlation of Sturtian diamictite successions in southern Australia and northwestern Tasmania by Re-Os black shale geochronology and the ambiguity of Sturtian-type diamictite-cap carbonate pairs as chronostratigraphic marker horizons. Precambrian Research 172, 301–310.

Kunzmann, M., Halverson, G. P., Scott, C. T., Minarik, W. G., Wing, B. A., 2015. Geochemistry of Neoproterozoic black shales from Svalbard: Implications for oceanic redox conditions spanning Cryogenian glaciations. Chemical Geology 417, 383–393.

Leavitt, W. D., Halevy, I., Bradley, A. S., Johnston, D. T., 2013. Influence of sulfate reduction rates on the Phanerozoic sulfur isotope record. Proceeding of the National Academy of Sciences of the USA 110, 11244–11249.

Li, Z.-X., Evans, D. A. D., Halverson, G. P., 2013. Neoproterozoic glaciations in a revised global paleogeography from the break-up of Rodinia to the assembly of Gondwanaland. Sedimentary Geology 294, 219–232.

Luepke, J. J., Lyons, T. W., 2001. Pre-Rodinian (Mesoproterozoic) supercontinental rifting along the western margin of Laurentia: geochemical evidence from the Belt-Purcell Supergroup. Precambrian Research 111, 79–90.

Lyons, T. W., Luepke, J. J., Schreiber, M. E., Zieg, G. A., 2000. Sulfur geochemical constraints on Mesoproterozoic restricted deposition: lower Belt Supergroup, northwestern United States. Geochimica et Cosmochemica Acta 64 (3), 427–437.

Macdonald, F. A., Strauss, J. V., Sperling, E. A., Halverson, G. P., Narbonne, G. M., Johnston, D. T., Kunzmann, M., Schrag, D. P., Higgins, J. A., 2013. The stratigraphic

relationship between the Shuram carbon isotope excursion, the oxygenation of Neoproterozoic oceans, and the first appearance of the Ediacara biota and bilaterian trace fossils in northwestern Canada. Chemical Geology 362, 250–272.

MacNaughton, R. B., Narbonne, G. M., Dalrymple, R. W., 2000. Neoproterozoic slope deposits, Mackenzie Mountains, northwestern Canada: implications for passive margin development and Ediacaran faunal ecology. Canadian Journal of Earth Sciences 37 (7), 997–1020.

Maloof, A. C., Halverson, G. P., Kirschvink, J. L., Schrag, D. P., Weiss, B. P., Hoffman, P. F., 2006. Combined paleomagnetic, isotopic, and stratigraphic evidence for true polar wander from the Neoproterozoic Akademikerbreen Group, Svalbard, Norway. Geological Society of America Bulletin 118 (9/10), 1099–1124.

Narbonne, G. M., Aitken, J. D., 1995. Neoproterozoic of the Mackenzie Mountains, northwestern Canada. Pre 73, 101–121.

Pellerin, A., Bui, T. H., Rough, M., Mucci, A., Canfield, D. E., Wing, B. A., 2015. Mass-dependent sulfur isotope fractionation during reoxidative sulfur cycling: A case study from Mangrove Lake, Bermuda. Geochimica et Cosmochemica Acta 149, 152–164.

Planavsky, N. J., McGoldrick, P., Scott, C. T., Li, C., Reinhard, C. T., Kelly, A. E., Chu, X., Bekker, A., Love, G. D., Lyons, T. W., 2011. Widespread iron-rich conditions in the mid-Proterozoic ocean. Nature 477, 448–451.

Poulton, S. W., Canfield, D. E., 2011. Ferruginous conditions: A dominant feature of the ocean through Earth's history. Elements 7, 107–112.

Rooney, A. D., Macdonald, F. A., Strauss, J. V., Dudás, F. Ö., Hallmann, C., Selby, D., 2014. Re-Os geochronology and coupled Os-Sr isotope constraints on the Sturtian snowball Earth. Proceedings of the National Academy of Sciences of the USA 111 (1), 51–56.

Rosman, K. J. R., Taylor, P. D. P., 1998. Isotopic compositions of the elements 1997. Pure and Applied Chemistry 70 (1), 217–235.

Sansjofre, P., Cartigny, P., Trindade, R. I. F., Nogueira, A. C. R., Agrinier, P., Ader, M., 2016. Multiple sulfur isotope evidence for massive oceanic sulfate depletion in the aftermath of Snowball Earth. Nature Communications, doi:10.1038/ncomms12192.

Schieber, J., 1989. Facies and origin of shales of the mid-Proterozoic Newland Formation, Belt Basin, Montanta, USA. Sedimentology 36, 203–219.

Scott, C. T., Wing, B. A., Bekker, A., Planavsky, N. J., Medvedev, P., Bates, S. M., Yun, M., Lyons, T. W., 2014. Pyrite multiple-sulfur isotope evidence for rapid expansion and contraction of the early Paleoproterozoic seawater sulfate reservoir. Earth and Planetary Science Letters 389, 95–104.

Sears, J. W., Chamberlain, K. R., Buckley, S. N., 1998. Structural and U-Pb geochronological evidence for 1.47 Ga rifting in the Belt basin, western Montana. Canadian Journal of Earth Sciences 35, 467–475.

Sim, M. S., Bosak, T., Ono, S., 2011a. Large sulfur isotope fractionation does not require disproportionation. Science 333, 74–77.

Sim, M. S., Ono, S., Donovan, K., Templer, S. P., Bosak, T., 2011b. Effect of electron donors on the fractionation of sulfur isotopes by a marine *Desulfovibrio* sp. Geochimica et Cosmochemica Acta 75 (15), 4244–4259.

Sperling, E. A., Halverson, G. P., Knoll, A. H., Macdonald, F. A., Johnston, D. T., 2013. A basin redox transect at the dawn of animal life. Earth and Planetary Science Letters 271–372, 143–155.

Winston, D., 1986. Sedimentation and tectonics of the Middle Proterozoic Belt basin and their influence on Phanerozoic compression and extension in western Montana and northern Idaho. In: Peterson, J. A. (Ed.), Paleotectonics and Sedimentation in the Rocky Mountain Region, United States. AAPG Memoir 41, American Association of Petroleum Geologists.

Winston, D., 1990. Evidence for intracratonic, fluvial and lacustrine settings of Middle and

Late Proterozoic basins of western USA. In: 535-564 (Ed.), Mid-Proterozoic Laurentia-Baltica. Geological Association of Canada Special Paper 38.

Winston, D., Link, P. K., 1993. Middle Proterozoic rocks of Montana, Idaho and eastern Washington: The Belt Supergroup. In: Reed, J. C. (Ed.), Precambrian: Conterminous US: The Geology of North America. pp. 487–517.